Langmuir

Article

pubs.acs.org/Langmuir

Numerical Simulations of the Digital Microfluidic Manipulation of Single Microparticles

Chuanjin Lan,[†] Souvik Pal,[†] Zhen Li,[‡] and Yanbao Ma*[,†]

[†]School of Engineering, University of California—Merced, Merced, California 95343, United States

[‡]Division of Applied Mathematics, Brown University, Providence, Rhode Island 02912, United States

Supporting Information

ABSTRACT: Single-cell analysis techniques have been developed as a valuable bioanalytical tool for elucidating cellular heterogeneity at genomic, proteomic, and cellular levels. Cell manipulation is an indispensable process for single-cell analysis. Digital microfluidics (DMF) is an important platform for conducting cell manipulation and single-cell analysis in a high-throughput fashion. However, the manipulation of single cells in DMF has not been quantitatively studied so far. In this article, we investigate the interaction of a single microparticle with a liquid droplet on a flat substrate using numerical simulations. The droplet is driven by capillary force generated from the wettability gradient of the substrate. Considering the Brownian motion of microparticles, we utilize many-body dissipative particle dynamics (MDPD), an off-lattice mesoscopic simulation technique, in this numerical study. The manipulation processes (including pickup, transport, and drop-off) of a single microparticle with a liquid droplet are simulated. Parametric studies are conducted to investigate the effects on the manipulation processes from the droplet size, wettability gradient, wetting properties of the microparticle, and particle−substrate friction coefficients. The numerical results show that the pickup, transport, and drop-off processes can be precisely controlled by these parameters. On the basis of the numerical results, a trap-free delivery of a hydrophobic microparticle to a destination on the substrate is demonstrated in the numerical simulations. The numerical results not only provide a fundamental understanding of interactions among the microparticle, the droplet, and the substrate but also demonstrate a new technique for the trap-free immobilization of single hydrophobic microparticles in the DMF design. Finally, our numerical method also provides a powerful design and optimization tool for the manipulation of microparticles in DMF systems.

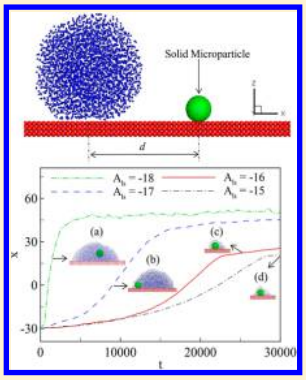

I. INTRODUCTION

Single-cell analysis (SCA) has attracted increased research interest because of its capability to decipher individual cells at genomic, proteomic, and cellular levels within a heterogeneous cell population.[1−3] The manipulation of individual cells in a small volume of liquid is of critical importance in SCA,[4] and digital microfluidics (DMF) is an emerging liquid-handling technology that enables precise control of individual picoliter liquid droplets and the manipulation of isolated cells in a high-throughput fashion.[5−7]

Currently, the design of DMF for the manipulation of individual cells is mainly based on a trial-and-error method. The fundamental understanding of interactions among microparticles (including cells), droplets, and substrates is of critical importance to the design and optimization of the DMF system for the SCA. Without considering the manipulation of microparticles, the flow dynamics in the DMF system has been studied extensively in both experiments and numerical simulations. Moumen et al.[8] performed experiments on the motion of droplets on a horizontal surface with a wettability gradient and found that the velocity of a droplet was a strong function of position along the wettability gradient. Kinoshita et al.[9] and Lu et al.[10] used microparticle image velocimetry (μ-PIV) for the internal flow measurement of a droplet and reconstructed the 3D velocity field from the 2D μ-PIV experimental data. Ma et al.[11] reported an experimental investigation of a flow field inside droplets, showing that the capillary number and droplet geometry had no effect on the observed flow dynamics. Except for experimental studies, the flow dynamics in DMF systems has been studied numerically using many-body dissipative particle dynamics (MDPD),[12−19] a special form of the dissipative particle dynamics (DPD) method with a consideration of liquid−vapor coexistence.[20] DPD is a particle-based mesoscopic simulation method that is similar to coarse-grained molecular dynamics (MD) simulations. However, compared to MD simulations, the DPD approach can capture physical phenomena occurring on temporal and spatial scales many orders of magnitude larger. Also, unlike the continuous deterministic approach based on the Navier−Stokes solver, DPD is a stochastic approach that can take the Brownian motion of fluid/solid particles into account.

While the manipulation of liquid droplets has been extensively studied, the manipulation of microparticles with liquid droplets has not been quantitatively studied so far. To fill this knowledge gap, we conduct a numerical study of the manipulation of single microparticles with a liquid droplet

Received: June 1, 2015
Revised: July 26, 2015
Published: August 4, 2015

DOI: 10.1021/acs.langmuir.5b02011
Langmuir 2015, 31, 9636−9645

driven by the capillary force generated from the wettability gradient of the substrate. To consider the moving triple line and the Brownian motion of microparticles, we utilize MDPD to investigate the interaction of a single microparticle with a liquid droplet on a flat substrate. We will mainly focus on the manipulation processes of a single microparticle with a droplet, including pickup, transportation, and drop-off. The rest of this article is organized as follows: the algorithms of DPD and MDPD approaches are described in section II; the numerical results on the manipulation of the microparticle are shown in section III, followed by conclusions given in section IV.

II. NUMERICAL METHOD

In this section, we describe the DPD and MDPD methods, the modeling of the wettability gradient in MDPD, and the modeling of a microparticle and its interaction with the substrate.

II.1. Algorithms of DPD and MDPD. DPD is a mesh-free particle-based method in which the fluid is modeled as a group of beads.[21] The motion of DPD beads is governed by Newton's second law given by

$$\frac{\mathrm{d}\vec{r}_i}{\mathrm{d}t} = \vec{v}_i \tag{1}$$

$$m_i\frac{\mathrm{d}\vec{v}_i}{\mathrm{d}t} = \vec{f}_i = \sum_{i\neq j}\left(\vec{F}_{ij}^{\mathrm{C}} + \vec{F}_{ij}^{\mathrm{D}} + \vec{F}_{ij}^{\mathrm{R}}\right) \tag{2}$$

where $\vec{r}_i$, $\vec{v}_i$ and $\vec{f}_i$ denote the ith bead's position, velocity, and total force exerted on the bead, respectively. The three components of $\vec{f}_i$, including the conservative force $\vec{F}_{ij}^{\mathrm{C}}$, dissipative force $\vec{F}_{ij}^{\mathrm{D}}$, and random force $\vec{F}_{ij}^{\mathrm{R}}$, are given by[21]

$$\vec{F}_{ij}^{\mathrm{C}} = \alpha\omega_{\mathrm{C}}(r_{ij})\vec{e}_{\mathrm{ij}} \tag{3}$$

$$\vec{F}_{ij}^{\mathrm{D}} = -\gamma\omega_{\mathrm{D}}(r_{ij})(\vec{e}_{ij}\cdot\vec{v}_{ij})\vec{e}_{ij} \tag{4}$$

$$\vec{F}_{ij}^{\mathrm{R}} = \varphi\omega_{\mathrm{R}}(r_{ij})\,\theta_{ij}(\delta_t)^{-1/2}\vec{e}_{ij} \tag{5}$$

where $r_{ij} = |\vec{r}_{ij}|$, $\vec{r}_{ij} = \vec{r}_i - \vec{r}_j$, $\vec{e}_{ij} = \vec{r}_{ij}/r_{ij}$ and $\vec{v}_{ij} = \vec{v}_i - \vec{v}_j$. ω_{C}, ω_{D}, and ω_{R} are weight functions for conservative, dissipative, and random forces, respectively. θ_{ij} is the Gaussian white noise with zero mean and unit variance. α, γ, and φ are the amplitudes of conservative, dissipative, and random forces, respectively. The dissipative and random forces act as a thermostat if the weight functions and amplitudes are chosen to obey the fluctuation−dissipation theorem[22]

$$\omega_{\mathrm{D}}(r) = [\omega_{\mathrm{R}}(r)]^2 \tag{6}$$

$$\varphi^2 = 2\gamma k_{\mathrm{B}}T \tag{7}$$

where k_{B} is the Boltzmann constant and T is the temperature of the system. The weight functions are commonly chosen as[21]

$$\omega_{\mathrm{C}}(r_{ij}) = \begin{cases} 1 - r_{ij}/r_{\mathrm{c}}, & (r < r_{\mathrm{c}}) \\ 0, & (r \geq r_{\mathrm{c}}) \end{cases} \tag{8}$$

$$\omega^{\mathrm{D}}(r) = [\omega^{\mathrm{R}}(r)]^2 = \begin{cases} \left(1 - \frac{r_{ij}}{r_{\mathrm{c}}}\right)^2, & (r < r_{\mathrm{c}}) \\ 0, & (r \geq r_{\mathrm{c}}) \end{cases} \tag{9}$$

To consider liquid−vapor coexistence, Warren[20] proposed a MDPD method. In the MDPD approach, the density-dependent conservative force was introduced empirically with a cutoff range of $r_{\mathrm{d}} = 0.75r_{\mathrm{c}}$

$$\vec{F}_{ij}^{\mathrm{C}} = A_{ij}\omega_{\mathrm{C}}(r_{ij}) + B_{ij}(\bar{\rho}_i + \bar{\rho}_j)\,\omega_{\mathrm{d}}(r_{ij}) \tag{10}$$

where A_{ij} and B_{ij} are amplitudes of attractive and repulsive forces, respectively, and

$$\omega_{\mathrm{d}}(r_{ij}) = \begin{cases} 1 - r_{ij}/r_{\mathrm{d}}, & (r < r_{\mathrm{d}}) \\ 0, & (r \geq r_{\mathrm{d}}) \end{cases} \tag{11}$$

The repulsive part depends on a weighted average of bead density, and the attractive part is density-independent. The density for each bead is defined as[20]

$$\bar{\rho}_i = \sum_{i\neq j} 15/(2\pi r_{\mathrm{d}}^3)(1 - r_{ij}/r_{\mathrm{d}})^2 \tag{12}$$

The MDPD parameters are chosen from previous studies,[15,18,20] as listed in Table 1. In this table, B_{ll} represents the repulsion between liquid (l) beads, while B_{lw} represents the repulsion between the substrate wall (w) and liquid (l) beads. In the present work, dimensionless variables are introduced to carry out the simulations and interpret the results. In particular, a solid microparticle of 10 μm is considered, and the length of the MDPD system is normalized by L = 10 μm. The corresponding mass unit is $m = 1.67 \times 10^{-13}$ kg at a particle number density of $\rho = 6.0$, which gives a liquid density of 1.0×10^3 kg/m^3. The time unit is chosen as $t = 4.15$ μs so that the surface tension $\sigma = 7.53$ in the MDPD system corresponds to a liquid−vapor surface tension of 0.073 N/m. Unless otherwise specified, all of the variables in the present article are normalized by the length, mass, and time units, and the results are interpreted in reduced units.

Table 1. Computational Parameters Used in MDPD Simulations

parameters	symbol	value
fluid bead density	ρ	6.00
cut-off radius of attractive force	r_{c}	1.00
cut-off radius of repulsive force	r_{d}	0.75
amplitude of random force	φ	6.00
attraction parameter	A_{ll}	−40.00
repulsion parameter	$B_{\mathrm{ll}} = B_{\mathrm{lw}}$	25.00
time step	Δt	0.01

II.2. Modeling of the Wettability Gradient. The droplet is driven by the capillary force generated from the wettability gradient of the substrate. The wettability of the substrate wall surface is characterized by a contact angle θ ranging from 0 to 180°. When θ is less than 90°, the surface is hydrophilic. Otherwise, it is hydrophobic. In MDPD, the wettability property is modeled by an attraction parameter A_{lw} between a liquid bead from the droplet and a solid bead from the substrate. To build the relationship between the static contact

DOI: 10.1021/acs.langmuir.5b02011
Langmuir 2015, 31, 9636−9645

angle θ and attraction parameter A_{lw}, we conduct numerical simulations of a droplet with a radius of 12 resting on a substrate with a flat wall surface. In the MDPD simulations, the substrate is composed of three layers of frozen solid beads. A periodic boundary condition is applied in both the x and y horizontal directions that are parallel to the substrate surface. To avoid the penetration of liquid beads into the substrate, a bounce-forward reflection boundary condition is used for the interface between the droplet and the substrate. The temporal integration of MDPD equations is performed using a modified velocity Verlet algorithm.[21] Compared to the forces in eq 2, the gravitational force is negligible. All other parameters are specified in Table 1. In total, 16 cases with A_{lw} spanning from −22 to −7 with an increment of 1 are considered. For each case, the contact angle of the droplet is calculated on the basis of the convergent results. Figure 1 shows the relation of θ versus A_{lw}.

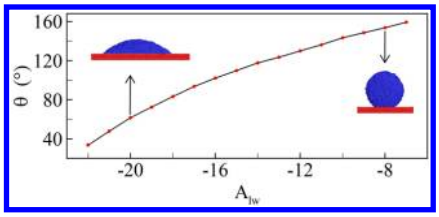

Figure 1. Relationship between static contact angle θ and liquid wall interaction parameter A_{lw}. An error bar is not shown since the error is always less than 1%.

The substrate surface is hydrophilic if A_{lw} is less than −17.18. It becomes hydrophobic if A_{lw} is greater than −17.18. On the basis of the results shown in Figure 1, a location-dependent A_{lw} is specially designed to make contact angle θ change linearly in the x direction

$$A_{lw} = \begin{cases} -8.77, x < x_0 \\ -1.21 - \sqrt{57.08 + 3.30\dfrac{\theta_0 - \theta_f}{(x_f - x_0)}(x - x_0)}, x_0 \le x \le x_f \\ -21.71, x > x_f \end{cases} \quad (13)$$

where x_0 and x_f are the initial position (hydrophobic end) and final position (hydrophilic end) of the region with the wettability gradient. Figure 2 shows the shapes of a droplet at

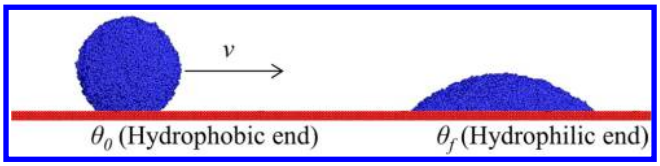

Figure 2. Motion of a liquid droplet on a substrate with a wettability gradient.

the hydrophobic end with static contact angle $\theta_0 = 150°$ and at the hydrophilic end with static contact angle $\theta_f = 40°$, respectively. When a droplet is placed between x_0 and x_f, a capillary force will be generated due to the asymmetric contact angle across the droplet.[23−25] Consequently, the droplet will be driven along the decreasing contact angle direction. The validation of MDPD modeling of a droplet driven by a wettability gradient was reported in our previous work.[18] Here, we extend the MDPD model to the study of the manipulation of single microparticles with a droplet.

II.3. Modeling of Microparticles. In DPD simulations involving liquid/solid interactions, both liquid and solid are modeled as soft beads that allow overlap and penetration between different beads. There are two schemes reported in the literature to avoid the penetration of liquid beads into solid microparticles. The first scheme is to configure solid DPD beads in a face-centered-cubic (fcc) lattice via rigid or superstrong bonds.[26−29] The fcc lattice constant of the solid beads is adjusted to avoid the undesirable penetration of liquid beads into the solid ones. The second scheme is to model the microparticle as a hollow sphere with sufficient density of solid beads packed on the surface. The high density of solid beads can efficiently repel liquid beads from penetrating the microparticles.[30,31]

However, in the MDPD approach, there is an attractive force between liquid beads and solid microparticle based on eq 10. The attractive force can always induce some penetration of liquid beads into the microparticle. To solve this problem, we uniformly configure 612 solid beads on the microsphere surface and apply a specular reflection boundary condition at the liquid-microsphere interface.[32] Once a liquid bead penetrates the microparticle, the liquid bead is specularly reflected back from the microparticle surface. The microparticle moves as a rigid sphere, and the motion can be decomposed into two independent modes: translation and rotation, which can be determined by the total force and torque exerted on the entire microparticle. After the total force and torque acting on the entire microparticle are calculated by summing forces and torques on each bead composing the microparticle, the translational motion and rotational motion of the microparticle are integrated independently.[33,34]

After dealing with interactions between liquid beads and microparticles in the MDPD scheme, we need to model the interaction between the microparticle and the substrate surface. On the basis of a solid−solid contact model reported by Johnson et al.,[35] we assume that the substrate material is elastic and the spherical microparticle is rigid. The depth of indentation d_{in} is related to the load (normal force) by

$$d_{in} = \left(\frac{9F_{normal}^2}{16R_sE^2}\right)^{1/3} \quad (14)$$

where F_{normal} is the normal force, E is the elastic modulus of the substrate, and R_s is the radius of a solid microparticle. The microparticle is attached to the wall due to the adhesion force that is determined by summing all of the forces exerted on the microparticle beads from the substrate. This adhesion force is balanced by the normal force that is determined from the elastic indentation of the substrate (eq 14). Meanwhile, once there is contact with the substrate wall, the rolling motion around the contact point will replace the free rotational motion for a suspended microparticle. Rolling friction force and kinetic friction force on microparticles are taken into consideration by multiplying the normal force with a rolling friction coefficient f_r and a static friction coefficient f_s, respectively.

II.4. Configuration and Parameters of MDPD Simulations. After the numerical model is built, the interactions among the liquid droplet (l), the substrate wall (w), and solid microparticle (s) can be simulated, with the initial setup at $t = 0$ shown in Figure 3. R_l is the radius of the liquid droplet, R_s is the radius of solid microparticle, and d is the initial distance

DOI: 10.1021/acs.langmuir.5b02011
Langmuir 2015, 31, 9636−9645

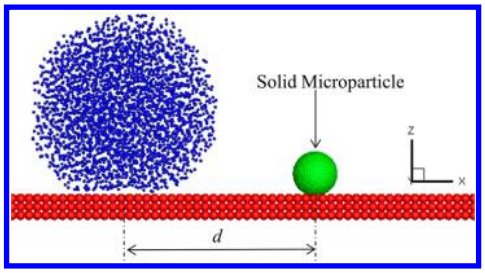

Figure 3. Initial setup of the liquid droplet (blue) and solid microparticle (green) resting on the substrate (red). d is the initial distance between the droplet and microparticle.

between the droplet and microparticle. The simulations are performed in a three-dimensional computational domain of size 150 (x) × 70 (y) × 20 (z). The origin point is set at the center of the computational domain. The starting position of the wettability gradient region is set as $x_0 = -40$, which is also the initial position of the liquid droplet center. The wall surface is set at $z = -10$, and other unchanged parameters are shown in Table 2. Besides these parameters mentioned above, the effects

Table 2. Parameters for Modeling the Microparticle and Wettability Gradient

parameters	symbol	value
elastic modulus of wall	E	1.0×10^6
initial position of liquid droplet	x_0	−40.0
attraction parameter with the substrate wall	A_{sw}	−1.0
repulsion parameter with liquid	B_{ls}	3.0
radius of solid microparticle	R_s	1.0
contact angle at hydrophobic end	θ_0	150.0°
contact angle at hydrophilic end	θ_f	40.0°
initial distance between droplet and microparticle	d	10.0

of remaining parameters on the manipulation of microparticle are investigated through parametric studies. These parameters include the droplet radius R_l, friction coefficients f_r and f_s, wettability gradient (by changing end position x_f), and attraction parameter between liquid beads and microparticle beads A_{ls}, which determines the wettability of the microparticle. The simulation results are discussed in the next section.

III. RESULTS AND DISCUSSION

At first, a baseline case for the pickup and transport of a hydrophobic microparticle by a droplet is simulated and analyzed in subsection III.1. Here are parameters used in the baseline case: droplet radius $R_l = 5$, wettability of the microparticle beads $A_{ls} = -15$, rolling friction coefficient $f_r = 0.1$, static friction coefficient $f_s = 0.2$, wettability gradient region end position $x_f = 40$, initial location of the droplet $x = -40$, and initial location of the microparticle $x = -30$. Then, we change one parameter and fix all other parameters as those in the baseline case to study the effects on the pickup and transport process from different parameters. The results are discussed in subsection III.2. After that, the microparticle drop-off process is studied in subsection III.3. Finally, a controlled trap-free delivery of hydrophobic microparticle is demonstrated in subsection III.4. For the convenience of discussion, reduced units are used.

III.1. Pickup and Transport of a Single Microparticle.

The flow physics in the manipulation of the droplet driven by the wettability gradient was reported in our previous work.[18] Here we mainly focus on the manipulation of the microparticle. Movie 01 in the Supporting Information shows the pickup and transport process of the microparticle by the droplet in the baseline case. When the droplet moves along the wettability-increasing direction (x direction), its front side comes into contact with the microparticle first. Then, the microparticle gradually gets submerged in the droplet. Due to the adhesion and friction between the microparticle and the substrate, the microparticle remains on the substrate until most of the droplet bypasses the microparticle. Finally, the microparticle is picked up and transported by the droplet. Figure 4 shows the droplet

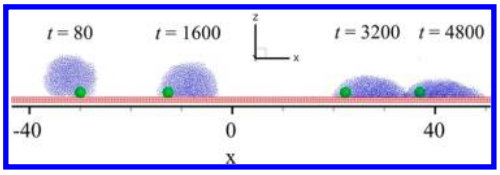

Figure 4. Shape and location of the droplet and microparticle at four different times: t = 80, 1600, 3200, and 4800.

shape and position as well as microparticle position at four different times: t = 80, 1600, 3200, and 4800. At t = 80, the microparticle is submerged in the droplet but remains at its original position of $x = -30$. At t = 1600, 3200, 4800, the microparticle is carried on by the droplet moving from the hydrophobic to hydrophilic region. During the whole transport process, the microparticle always stays near the vapor/liquid interface in the receding region of the droplet and stays in contact with the substrate. The simulation results on the transport of a single hydrophobic microparticle are consistent with the experimental observation of the transport of superhydrophobic PTFE particles as reported by Zhao and Cho.[37] Due to the friction between the microparticle and substrate, the droplet is significantly decelerated. Without the microparticle, the travel time for the droplet from $x = -40$ to 40 is 2250. With the microparticle, the travel time increases to 4800. The travel time history of the microparticle sampled by every 50 000 time steps (Δt = 0.01, t_{sample} = 500) is shown in Figure 5. It shows that the z position of the microparticle

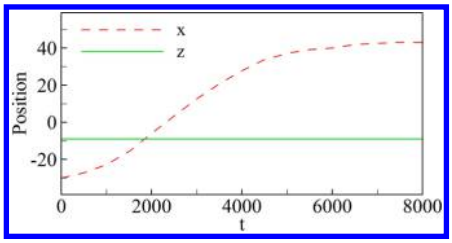

Figure 5. Travel time history of the microparticle.

remains almost constant at $z = -9$ even though there is oscillation due to the Brownian motion of the microparticle and stochastic interaction between the droplet and the microparticle. The x-position curve of the microparticle is composed of two segments: a concave (upward) segment and a convex (concave downward) segment. The microparticle is accelerated in the concave upward segment while it is decelerated in the convex segment. There exists an inflection point between t = 2000 and 4000. After passing $x = 40$ at t = 4800, the velocity of the droplet gradually decreases to zero due to friction and a lack of driving force.

DOI: 10.1021/acs.langmuir.5b02011
Langmuir 2015, 31, 9636−9645

III.2. Effects of Different Factors on the Pickup and Transport of the Microparticle. In this subsection, the effects on the pickup and transport of the microparticle from different parameters are studied and discussed. These parameters include droplet radius R_l, wettability gradient (determined by x_f), attraction parameter A_{ls}, and friction coefficients f_r and f_s.

III.2.1. Effect on the Transport of the Microparticle from the Droplet Size. The effect of droplet size on the manipulation of a single microparticle is discussed in this subsection. Figure 6

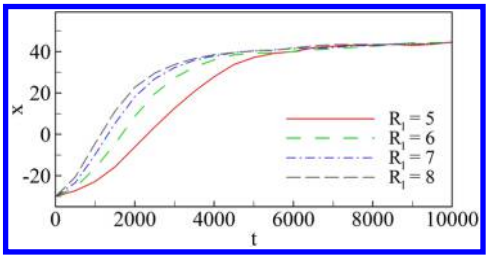

Figure 6. Time history of the microparticle position for different droplet sizes.

shows the time history of microparticle movement (in term of the x position of the microparticle center) at four different droplet sizes, i.e., R_l = 5, 6, 7, and 8, respectively. The travel time for the microparticle from $x = -30$ to 0 is shortened from 2317 to 1673, 1324, and 1140 as the droplet radius increases from 5 to 6, 7, and 8. This is because, for a larger droplet, the difference in wettability across the droplet is larger due to a larger contact surface between the droplet and substrate.[18] For $R_l \geq 8$, the effect on the manipulation of the microparticle from the droplet size becomes negligible, which is not shown here.

III.2.2. Effect on the Transport of the Microparticle from the Wettability Gradient. The effect of different wettability gradients is studied by varying the end position of the wettability gradient region x_f while maintaining static contact angles θ_0 =150° and θ_f = 40°. Here, the initial positions of microparticles for three different cases (x_f = 0, 20, and 40) are slightly adjusted to keep the same static contact angle of the droplet when the droplet moves to these positions. The results are shown in Figure 7. For all three cases, the microparticle is

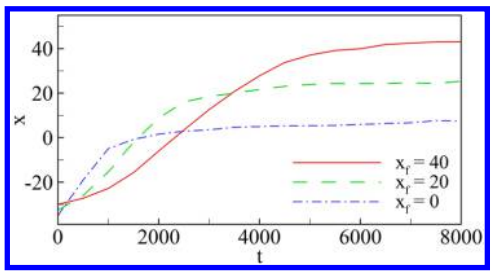

Figure 7. Time history of the microparticle position for different wettability gradients.

successfully picked up by the droplet and transported to the end of the wettability gradient region. For a higher wettability gradient (or smaller x_f), there is faster transport of the microparticle due to a larger driving force exerted on the droplet.

III.2.3. Effect on the Transport of the Microparticle from the Wettability of the Microparticle. As shown in Figure 1, the contact angle is 90° at $A_{ls} = -17.18$, and the surface wettability of the microparticle can be changed from hydrophobic to hydrophilic by decreasing the value of A_{ls}. Figure 8 shows the

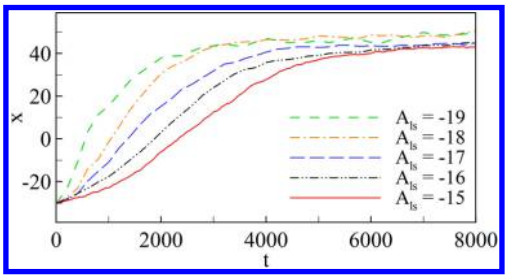

Figure 8. Time history of the microparticle x position with different wettability parameters A_{ls}.

time history of the manipulation of the microparticle for five different values of $A_{ls} = -15, -16, -17, -18$, and -19 (the corresponding contact angles are 110°, 102°, 93.5°, 83.5°, and 72.5°, respectively). It is found that there is faster transport of more hydrophilic microparticles. For $A_{ls} = -19$, the travel time of a droplet with a microparticle over the whole region with a wettability gradient is almost the same as that without the microparticle.

To explain different transport times of the microparticles with different wettabilities shown in Figure 8, the time history of vertical (z) positions of the microparticle center is compared in Figure 9 for different wettability parameters. It is found that

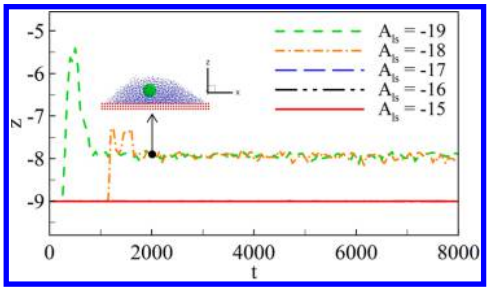

Figure 9. Time history of z position of the microparticle center with different wettability parameters. The inset shows that the microparticle is lifted up from the substrate surface.

the final z positions of the microparticle center remain at $z = -9$ for three cases with $A_{ls} \leq -17$. For the two cases with $A_{ls} = -18$ and -19, the final z positions of the microparticle center are lifted up to $z = -8$. For these two cases, there is oscillation in the z positions of the microparticle center due to Brownian motions of the microparticle as well as stochastic interactions with liquid beads. The inset of Figure 9 shows the shape of the droplet and the relative position of the microparticle at t = 2000 for $A_{ls} = -19$. For $A_{ls} = -19$, there is a sudden rise in the z position (up to $z = -5.5$) at t = 255, and then the microparticle center gradually returns to about $z = -8$ and remains around this level after t = 1000. For $A_{ls} = -18$, there is also a similar sudden rise in the microparticle in the z direction, but it occurs much later at t = 1153. Before the microparticle is lifted up, it is pulled forward on the substrate surface by the droplet. Because the friction between the microparticle and the substrate lasts longer in the $A_{ls} = -18$ case than in the $A_{ls} = -19$ case, there is faster transport of the microparticle in the $A_{ls} = -19$ case (Figure 8). For $A_{ls} = -15$, -16, and -17, the microparticle stays almost constant around $z = -9$, implying that it is always

DOI: 10.1021/acs.langmuir.5b02011
Langmuir 2015, 31, 9636−9645

attached on the substrate surface. The time-averaged values of the z position during the whole transport process are −9.00249 for A_{ls} = −15, −9.00216 for A_{ls} = −16, and −9.00170 for A_{ls} = −17. The slightly higher z position for higher A_{ls} (amplitudes of attractive force in eq 10) results from a stronger attractive force between the droplet and the microparticle. The overall attractive force slightly lifts up the microparticle in the z direction. Though the difference in z position is quite small for three different cases, the small difference in z position can lead to a large difference in the normal force due to the strong elastic modulus of the substrate. The higher z position of the microparticle will lead to a smaller normal force and a smaller friction for the motion of the microparticle. Consequently, a smaller friction will result in faster transport. This explains why there is faster transport of the microparticle among the three cases with A_{ls} = −15, −16, and −17, as shown in Figure 8. When A_{ls} decreases to less than −18, the attractive force between the droplet and the microparticle is strong enough to pull the microparticle away from the substrate surface, so the friction between the microparticle and the substrate disappears.

III.2.4. Effect on the Transport of the Microparticle from the Friction Coefficients. Six different combinations of f_s (0.2, 0.4, 0.8, and 1.6) and f_r (0.2, 0.4, and 0.8) are considered to study the effect of friction forces on the manipulation of the microparticle with a droplet, and all other parameters are same as those in the baseline case. The time history of x positions of the microparticle center for six cases is compared in Figure 10.

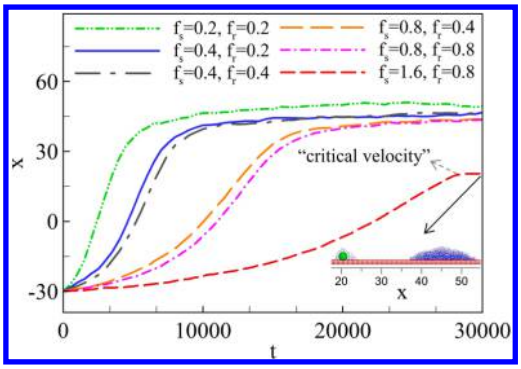

Figure 10. Variation of x position of the microparticle center with time using different friction coefficients. The inset shows the positions of the microparticle and droplet at t = 30 000 using f_s = 1.6 and f_r = 0.8.

The results show that there is a significant increase in the transport time of the microparticle when static friction coefficient f_s increases from 0.2 to 0.4, 0.8, and 1.6. For the same f_s (fixed at 0.4 or 0.8) the transport time of the microparticle is slightly increased when the rolling friction coefficient f_r gets doubled either from 0.2 to 0.4 for f_s = 0.4 or from 0.4 to 0.8 for f_s = 0.8. Because the manipulation of the microparticle is much more sensitive to the change in f_s than to that in f_r, only the effect of static friction coefficient f_s is discussed in the following text.

In cases f_s = 0.2, 0.4, and 0.8, the microparticle is picked up and transported to the end of the wettability gradient region, with more time used for a larger friction coefficient. When f_s is increased to 1.6, the microparticle is picked up by the droplet at the beginning. However, during the transport process, the microparticle is dropped off by the droplet and stays there with a few liquid beads attached (inset of Figure 10). The drop-off of the microparticle and the breakup of the droplet are related to the velocity of the droplet. There exists a threshold or critical velocity of the cargo droplet. Below the critical velocity, the droplet can carry the microparticle. Beyond the critical velocity, the instantaneous acceleration of the microparticle is less than that of the droplet, which will result in a velocity difference between the microparticle and the droplet. Finally, the microparticle is dropped off by the droplet, and some liquid enveloping the microparticle is separated from the main droplet and remains attached to the surface of the microparticle. Because the controlled drop-off is important to the manipulation of the microparticle, we will discuss the effect of different factors on the drop-off of microparticle in the next subsection.

III.3. Effects of Different Factors on the Dropoff of the Microparticle. In section III.2, we find that the droplet size, substrate wettability gradient, and microparticle wettability can strongly influence the pickup and transport of microparticles. As observed from Figure 10, strong friction (f_s = 1.6) results in the drop-off of the microparticle and breakup of the droplet. In order to control this process, we conduct a parametric study in order to achieve a better understanding of the drop-off and breakup mechanism, and the results are discussed below.

III.3.1. Effect on the Drop-Off of the Microparticle from the Droplet Size. With fixed A_{ls} = −15, x_f = 40, f_s = 1.6, and f_r = 0.8 and other parameters specified in Tables 1 and 2, we study the drop-off process with four different radii of droplets: R_l = 5, 6, 7, and 8. The results of transport processes for different radii of droplets are compared in Figure 11. For all four cases, the

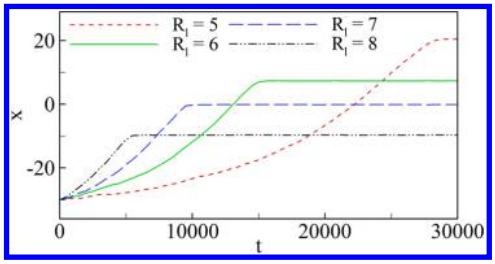

Figure 11. Time history of microparticle transport with different droplet sizes.

microparticle is dropped off before x = 40, where the wettability gradient ends. As the droplet size increases, there is earlier drop-off of the microparticle. This can be explained by the results of transport processes shown in Figure 6. With increasing droplet size, there is faster transport of the droplet as well as the microparticle due to the larger driving force generated from the wettability gradient. As a result, the critical velocity for the drop-off is reached earlier. On the basis of these results, the location where the microparticle is dropped off can be predicted and controlled with well-designed parameters, as implemented in the last section of this study.

III.3.2. Effect on the Drop-Off of the Microparticle from the Wettability Gradient. With A_{ls} = −15, R_l = 5, f_s = 1.6, and f_r = 0.8 and other parameters specified in Tables 1 and 2, we study the transport processes of the microparticle with three different wettability gradients controlled by x_f = 0, 20, and 40, respectively. The results of microparticle transport processes are compared in Figure 12. For the smallest wettability gradient with x_f = 40, the microparticle is dropped off at x = 20. When the wettability gradient increases, the drop-off position in terms of x decreases. The microparticle is completely dropped off for the two cases with x_f = 0 and 40 (Figure 12). However, an

DOI: 10.1021/acs.langmuir.5b02011
Langmuir 2015, 31, 9636−9645

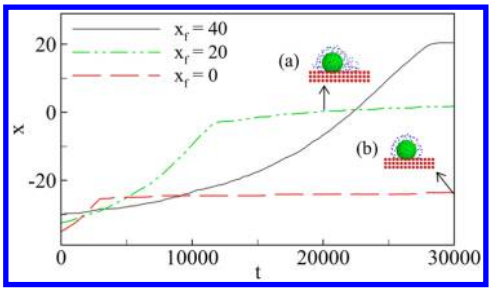

Figure 12. Time history of microparticle transport processes for three different wettability gradients. Inset (a): Satellite droplet attached to the microparticle for case $x_f = 20$ at $t = 20\,000$. Inset (b): Satellite droplet attached to the microparticle for case $x_f = 0$ at $t = 30\,000$.

interesting phenomenon is observed in the case with $x_f = 20$. After breaking up from the main droplet, the satellite droplet that envelopes the microparticle continues to move the microparticle toward the hydrophilic end at an extremely slow speed. Inset (a) in Figure 12 shows the shape of the satellite droplet for $x_f = 20$, which is different from that shown in inset (b) for $x_f = 0$. The volume of the satellite droplet will affect the controlled drop-off of the microparticle. When the volume of the satellite droplet is considerably small, the microparticle cannot be moved by the satellite droplet as shown in inset (b) of Figure 12. However, the microparticle can be moved by the satellite droplet if the volume of the satellite droplet is large enough (as shown in inset (a) of Figure 12).

III.3.3. Effect on the Drop-Off of the Microparticle from the Wettability of the Microparticle. With $R_l = 5$, $x_f = 40$, $f_s = 1.6$, and $f_r = 0.8$ and other parameters specified in Tables 1 and 2, we study the transport processes of the microparticle with four different values of A_{ls}, i.e., −15, −16, −17, and −18 (the corresponding contact angles are 110°, 102°, 93.5°, and 84.5°, respectively). The results of transport processes of the microparticle are compared in Figure 13. For both cases $A_{ls} = -18$ and −17, there is no breakup of the droplet during the transport processes. For the case with $A_{ls} = -18$, the hydrophilic microparticle is pulled away from the surface of the substrate so that the friction between the microparticle and the substrate surface disappears (inset (a) in Figure 13). For the case with $A_{ls} = -17$, the microparticle remains in contact

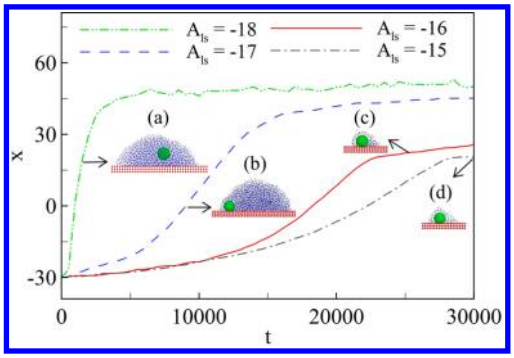

Figure 13. Time history of microparticle transport processes for different values of parameter A_{ls}. Inset (a): Relative position of the microparticle and the droplet in the case of $A_{ls} = -18$ at $t = 1650$. Inset (b): Relative position of the microparticle and the droplet in the case of $A_{ls} = -17$ at $t = 9050$. Inset (c): Satellite droplet attached to the microparticle in the case of $A_{ls} = -16$ at $t = 25\,500$. Inset (d): Satellite droplet attached to the microparticle in the case of $A_{ls} = -15$ at $t = 29\,500$.

with the substrate surface and stays in the receding region of the droplet during the transport process (inset (b) in Figure 13). Due to the friction between the microparticle and the substrate surface for the case with $A_{ls} = -17$, it takes a much longer time (7 times longer) for the microparticle to travel from $x = -30$ to 40 compared to that for the $A_{ls} = -18$ case. For the slightly hydrophobic microparticle with $A_{ls} = -16$ ($\theta = 102°$), the breakup of the microparticle and droplet happens at about the same x location but at an earlier time due to a larger transport velocity as compared to that of case $A_{ls} = -15$ (Figure 13). The satellite droplet in the case with $A_{ls} = -16$ continues to move the microparticle toward the hydrophilic end at a very slow speed (inset (c) in Figure 13). For the hydrophobic microparticle with $A_{ls} = -15$ ($\theta = 110°$), the volume of the satellite droplet is so small that it is unable to move the microparticle after separation from the main droplet. On the basis of the results shown in Figure 13, we find that the hydrophobic microparticles can be dropped off during the transportation process. For slightly hydrophobic microparticles (for example, $A_{ls} = -16$, $\theta = 102°$), the satellite droplet may continue to carry the microparticle and move forward with the driving force generated from the wettability gradient of the substrate. For hydrophobic microparticles with contact angles greater than 110°, the microparticles enveloped by satellite droplets will stay still on the substrate while the main droplet moves away. These results can be applied to the controlled trap-free delivery of hydrophobic microparticles, which is discussed in the next section.

III.4. Controlled Trap-Free Delivery of Hydrophobic Microparticles. As discussed in previous subsections, the transport and drop-off of the microparticle can be affected by the droplet size, the wettability gradient of the substrate, and also the wettability of the microparticle. On the basis of these results, a trap-free delivery of a hydrophobic microparticle ($A_{ls} = -15$) to a destination on the substrate with droplet cargo is demonstrated here. As in previous cases, the initial x positions of the droplet and the microparticle are −40 and −30, respectively. The designed location for the drop-off of the microparticle is between $x = -2$ and 2. The droplet size is chosen as $R_l = 5$, and frictions are chosen as $f_s = 0.8$ and $f_r = 0.4$, with other parameters the same as those specified in Tables 1 and 2.

To implement the controlled delivery of the microparticle, the whole process is divided into two stages. In stage 1, the droplet is driven in the x direction, and it picks up and transports the microparticle to a destination near $x = 0$. In stage 2, the microparticle is separated from the droplet and remains in the drop-off region ($-2 \le x \le 2$) while the droplet is moved away. For each stage, the wettability gradient of the substrate is specially designed.

In stage 1, wettability parameter A_{lw} is designed as

$$A_{lw} = \begin{cases} -16.66, & x \le -40 \\ -1.21 - \sqrt{420.11 + 4.54x}, & -40 < x \le 0 \\ -21.71, & 0 < x \le 2 \\ -1.21 - \sqrt{429.19 + 4.54x}, & x > 2 \end{cases} \quad (15)$$

The corresponding distribution of the contact angle is shown in Figure 14.

The key design of the wettability gradient of the substrate in stage 1 is to have a V-shaped distribution of the contact angle

DOI: 10.1021/acs.langmuir.5b02011
Langmuir 2015, 31, 9636−9645

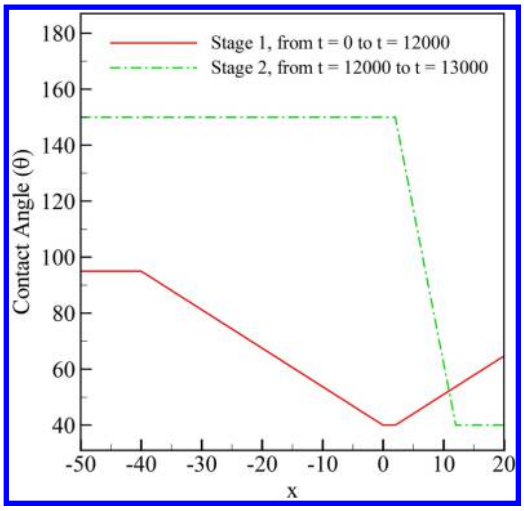

Figure 14. Distribution of the contact angle along the substrate in two stages.

with a valley near $x = 0$ so that the droplet and the microparticle will stop near $x = 0$. For $x \leq -40$, the contact angle remains constant at 95°. In the region of $-40 \leq x < 0$, the contact angle (θ) decreases linearly from 95° to 40°. A moderate wettability gradient is applied here for two reasons: (1) a large wettability gradient may lead to an unintended early drop-off of the microparticle before reaching its destination (section III.3.2); and (2) it takes a long time for controlled delivery with a small wettability gradient that generates only a weak capillary driving force. The reversed wettability gradient for $x > 2$ is designed to generate a capillary force pointing in the negative x direction, which functions as a break to stop the droplet movement. With this design, the droplet center is expected to stop at $x = 1$ due to the symmetry of the wettability gradient about that position. Because the hydrophobic microparticle tends to stay in the receding region of the droplet, the stopping position of the microparticle is expected to be around $x = -1$. The time assigned for stage 1 is 12 000, which is much longer than the droplet travel time (~8000) from $x = -40$ to 1. The extra-long time is to ensure that the droplet and the microparticle will completely stop at their designed locations.

The second stage is to separate the microparticle from the droplet while the microparticle is kept at around $x = 0$ as the droplet is moved away. On the basis of the results shown in Figure 12, depending on the wettability gradient, the volume of the satellite droplet that envelops the microparticle may be large enough to continue to move the microparticle away from the drop-off destination at around $x = 0$. This can be eliminated by using a strong wettability gradient. With the above consideration, a specially designed wettability distribution is given in stage 2:

$$A_{lw} = \begin{cases} -8.77, & x \leq 2 \\ -1.21 - \sqrt{-15.53 + 36.30x}, & 2 < x \leq 12 \\ -21.71, & x > 12 \end{cases} \quad (16)$$

The corresponding contact angle distribution is also plotted in Figure 14. For $x \leq 2$, the contact angle remains constant at 150°. In the region of $2 < x \leq 12$, the contact angle linearly decrease from 150° to 40°. For such a high wettability gradient, it is expected that the droplet will separate from the microparticle, and the satellite droplet enveloping the microparticle cannot move the microparticle due to its small volume. The time for stage 2 is from 12 000 to 13 000, which is long enough for the droplet to separate from the microparticle and move away.

Here, we assume the switching time for the surface wettability from stage 1 to stage 2 is extremely short so that the droplet shape will not change during the switching time. With this assumption, we conduct MDPD simulation for stages 1 and 2 while ignoring the switching time. The main purpose is to demonstrate the controlled delivery of the microparticle to the destination, including pickup, transport, and drop-off processes. Movie 02 in the Supporting Information shows the controlled delivery process based on the results of numerical simulations. Figure 15 shows the time history of the microparticle position. Three insets in Figure 15 show the shapes and positions of the microparticle and the droplet at three different times (t = 9000, 12 100, and 13 000 for insets (a–c), respectively). In stage 1, the microparticle is picked up by the droplet and transported to position $x = -2.3$. At t = 9000, the droplet and the microparticle completely stop, and their positions and status are shown in inset (a) of Figure 15. At t = 12 000, the wettability gradient suddenly changes from stage 1 to stage 2. A strong wettability gradient is imposed to quickly move away the droplet. Inset (b) in Figure 15 shows the status of the droplet and microparticle near the end of the separation at t = 12 100. The microparticle is dragged forward from $x = -2.3$ to -1.5 before the separation. After that, the main droplet moves while the microparticle enveloped by the satellite droplet is dropped off at $x = -1.5$ (inset (c) in Figure 15). Using precise control of the substrate wettability in two stages, we successfully demonstrate a trap-free delivery of the hydrophobic microparticle to a destination on the substrate with a droplet cargo in the numerical simulation.

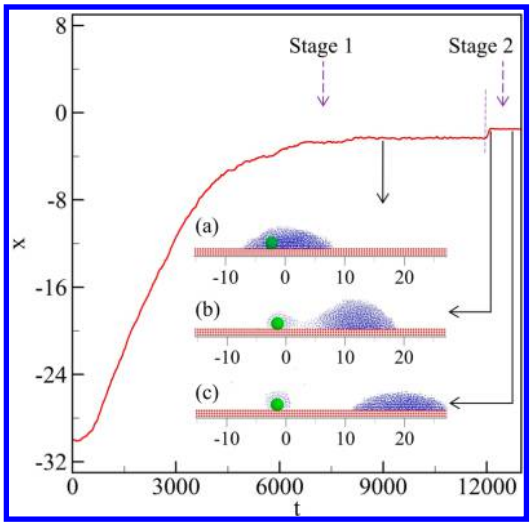

Figure 15. Time history of the manipulation of the microparticle with a droplet. Three insets show shapes and positions of the microparticle and the droplet at three different times: (a) t = 9000, (b) t = 12 100, and (c) t = 12 800. The droplet is shown in blue, and the solid microparticle is shown in green.

IV. CONCLUSIONS

In order to obtain a better understanding of the manipulation mechanisms of a single cell in digital microfluidic (DMF)

DOI: 10.1021/acs.langmuir.5b02011
Langmuir 2015, 31, 9636–9645

systems to facilitate single-cell analysis, we numerically studied the interaction among a solid microparticle, a solid substrate, and a liquid droplet using MDPD simulations. Driven by the capillary force generated from the wettability gradient on a substrate, the water droplet moves in the contact angle decreasing direction. The droplet can be used as a cargo to pick up, transport, and deliver a single microparticle to a designated destination. We conducted parametric studies to investigate the effects on the manipulation of the microparticle from the droplet size, gradient of the wettability, wetting properties of the microparticle, and particle−substrate friction coefficients. The results show that the microparticle manipulation processes are significantly affected by the droplet size, wettability gradient on the substrate surface, and particle−substrate friction coefficients. Specifically, when the droplet size is less than 8 times the microparticle size, the increase in the droplet size will speed up the microparticle delivery process. After the droplet size is more than 8 times the microparticle size, the effects of the droplet size on the manipulation of the microparticle become negligible. The wettability gradient provides the driving force for the manipulation of the microparticle, hence the increase in the wettability gradient can speed up the manipulation of microparticles. However, the increase in the particle−substrate friction coefficients can lead to unintentional drop-off of the microparticle during the transport process. The drop-off of the microparticle can be affected by the droplet size, the wettability gradient, and the wettability of the microparticle. On the basis of the numerical results, these sensitive parameters, including the droplet size, the wettability gradient on the substrate surface, and particle−substrate friction coefficients, can be used to guide the optimal design of DMF systems for the manipulation of single microparticles.

It is also found that the relative positions of the microparticle inside the droplet are different for hydrophobic and hydrophilic microparticles during the manipulation processes. For a hydrophobic microparticle, it remains in contact with the substrate surface in the receding region of droplet, which retards the transport process due to the friction between the microparticle and the substrate. For a hydrophilic microparticle, it is lifted up from the substrate surface so that the friction from the substrate disappears. Due to this difference, different strategies should be applied for the drop-off or separation of the microparticle from the droplet after the microparticle is delivered to the designed destination. For a hydrophobic microparticle, we demonstrated a trap-free delivery to a destination on the substrate with a droplet cargo through numerical simulations. The separation of a hydrophilic microparticle from the droplet is much more complicated than that of a hydrophobic microparticle, which will be a topic for future study.

This article reports the first numerical study of the manipulation of single microparticles with a droplet. The numerical results provide a fundamental understanding of interactions among the microparticle, the droplet, and the substrate to facilitate the optimal design of a DMF system for single-cell analysis. The MDPD method also provides a valuable numerical tool that can be used to guide the optimal design of DMF systems for the manipulation of microparticles. In particular, the trap-free delivery of a hydrophobic microparticle is demonstrated through numerical simulations, which provide a new technique for the manipulation of hydrophobic microparticles in the DMF design.

■ ASSOCIATED CONTENT

Supporting Information

The Supporting Information is available free of charge on the ACS Publications website at DOI: 10.1021/acs.langmuir.5b02011.

Descriptions of two movies showing the microparticle manipulation processes with a microdroplet (PDF)
Pickup and transport (ZIP)
Controlled delivery (ZIP)

■ AUTHOR INFORMATION

Corresponding Author

*E-mail: yma5@ucmerced.edu.

Author Contributions

C.L. performed numerical modeling of numerical simulations. All authors analyzed the data and contributed to the discussion and writing of this work.

Funding

We acknowledge financial support from a startup grant from UC Merced.

Notes

The authors declare no competing financial interest.

■ REFERENCES

(1) Huang, N. T.; Zhang, H. L.; Chung, M. T.; Seo, J. H.; Kurabayashi, K. Recent advancements in optofluidics-based single-cell analysis: optical on-chip cellular manipulation, treatment, and property detection. *Lab Chip* **2014**, *14* (7), 1230−1245.

(2) Tang, F. C.; Lao, K. Q.; Surani, M. A. Development and applications of single-cell transcriptome analysis. *Nat. Methods* **2011**, *8* (4), S6−S11.

(3) Junkin, M.; Tay, S. Microfluidic single-cell analysis for systems immunology. *Lab Chip* **2014**, *14* (7), 1246−1260.

(4) Kleparnik, K.; Foret, F. Recent advances in the development of single cell analysis-A review. *Anal. Chim. Acta* **2013**, *800*, 12−21.

(5) Choi, K.; Ng, A. H.; Fobel, R.; Wheeler, A. R. Digital microfluidics. *Annu. Rev. Anal. Chem.* **2012**, *5*, 413−440.

(6) Shih, S. C. C.; Gach, P. C.; Sustarich, J.; Simmons, B. A.; Adams, P. D.; Singh, S.; Singh, A. K. A droplet-to-digital (D2D) microfluidic device for single cell assays. *Lab Chip* **2015**, *15* (1), 225−236.

(7) Kumar, P.; Vriens, K.; Cornaglia, M.; Gijs, M.; Kokalj, T.; Thevissen, K.; Geeraerd, A.; Cammue, B.; Puers, R.; Lammertyn, J. Digital microfluidics for time-resolved cytotoxicity studies on single non-adherent yeast cells. *Lab Chip* **2015**, *15* (8), 1852−1860.

(8) Moumen, N.; Subramanian, R. S.; McLaughlin, J. B. Experiments on the motion of drops on a horizontal solid surface due to a wettability gradient. *Langmuir* **2006**, *22* (6), 2682−2690.

(9) Kinoshita, H.; Kaneda, S.; Fujii, T.; Oshima, M. Three-dimensional measurement and visualization of internal flow of a moving droplet using confocal micro-PIV. *Lab Chip* **2007**, *7* (3), 338−346.

(10) Lu, H.-W.; Bottausci, F.; Fowler, J. D.; Bertozzi, A. L.; Meinhart, C. A study of EWOD-driven droplets by PIV investigation. *Lab Chip* **2008**, *8* (3), 456−461.

(11) Ma, S.; Sherwood, J. M.; Huck, W. T.; Balabani, S. On the flow topology inside droplets moving in rectangular microchannels. *Lab Chip* **2014**, *14* (18), 3611−3620.

(12) Liu, M.; Meakin, P.; Huang, H. Dissipative particle dynamics with attractive and repulsive particle-particle interactions. *Phys. Fluids* **2006**, *18* (1), 017101.

(13) Tiwari, A.; Abraham, J. Dissipative-particle-dynamics model for two-phase flows. *Phys. Rev. E* **2006**, *74* (5), 056701.

(14) Huang, J.; Shu, C.; Chew, Y. Numerical investigation of transporting droplets by spatiotemporally controlling substrate wettability. *J. Colloid Interface Sci.* **2008**, *328* (1), 124−133.

DOI: 10.1021/acs.langmuir.5b02011
Langmuir 2015, 31, 9636−9645

(15) Cupelli, C.; Henrich, B.; Glatzel, T.; Zengerle, R.; Moseler, M.; Santer, M. Dynamic capillary wetting studied with dissipative particle dynamics. *New J. Phys.* **2008**, *10* (4), 043009.
(16) Das, A. K.; Das, P. K. Simulation of drop movement over an inclined surface using smoothed particle hydrodynamics. *Langmuir* **2009**, *25* (19), 11459−11466.
(17) Das, A.; Das, P. Multimode dynamics of a liquid drop over an inclined surface with a wettability gradient. *Langmuir* **2010**, *26* (12), 9547−9555.
(18) Li, Z.; Hu, G.-H.; Wang, Z.-L.; Ma, Y.-B.; Zhou, Z.-W. Three dimensional flow structures in a moving droplet on substrate: A dissipative particle dynamics study. *Phys. Fluids* **2013**, *25* (7), 072103.
(19) Wang, Y.; Chen, S. Numerical Study on Droplet Sliding across Micropillars. *Langmuir* **2015**, *31*, 4673−4677.
(20) Warren, P. B. Vapor-liquid coexistence in many-body dissipative particle dynamics. *Phys. Rev. E: Stat. Phys., Plasmas, Fluids, Relat. Interdiscip. Top.* **2003**, *68* (6), 066702.
(21) Groot, R. D.; Warren, P. B. Dissipative particle dynamics: bridging the gap between atomistic and mesoscopic simulation. *J. Chem. Phys.* **1997**, *107* (11), 4423−4435.
(22) Espanol, P.; Warren, P. Statistical mechanics of dissipative particle dynamics. *EPL (Europhysics Letters)* **1995**, *30* (4), 191−196.
(23) Yao, X.; Bai, H.; Ju, J.; Zhou, D.; Li, J.; Zhang, H.; Yang, B.; Jiang, L. Running droplet of interfacial chemical reaction flow. *Soft Matter* **2012**, *8* (22), 5988−5991.
(24) Bliznyuk, O.; Seddon, J. R.; Veligura, V.; Kooij, E. S.; Zandvliet, H. J.; Poelsema, B. Directional liquid spreading over chemically defined radial wettability gradients. *ACS Appl. Mater. Interfaces* **2012**, *4* (8), 4141−4148.
(25) Xu, X.; Qian, T. Droplet motion in one-component fluids on solid substrates with wettability gradients. *Phys. Rev. E* **2012**, *85* (5), 051601.
(26) Laradji, M.; Hore, M. J. Nanospheres in phase-separating multicomponent fluids: A three-dimensional dissipative particle dynamics simulation. *J. Chem. Phys.* **2004**, *121* (21), 10641−10647.
(27) Hore, M. J.; Laradji, M. Microphase separation induced by interfacial segregation of isotropic, spherical nanoparticles. *J. Chem. Phys.* **2007**, *126* (24), 244903.
(28) Huang, M.; Li, Z.; Guo, H. The effect of Janus nanospheres on the phase separation of immiscible polymer blends via dissipative particle dynamics simulations. *Soft Matter* **2012**, *8* (25), 6834−6845.
(29) Salib, I.; Yong, X.; Crabb, E. J.; Moellers, N. M.; McFarlin, G. T., IV; Kuksenok, O.; Balazs, A. C. Harnessing fluid-driven vesicles to pick up and drop off Janus particles. *ACS Nano* **2013**, *7* (2), 1224−1238.
(30) Fan, H.; Striolo, A. Nanoparticle effects on the water-oil interfacial tension. *Phys. Rev. E* **2012**, *86* (5), 051610.
(31) Luu, X.-C.; Yu, J.; Striolo, A. Nanoparticles adsorbed at the water/oil interface: coverage and composition effects on structure and diffusion. *Langmuir* **2013**, *29* (24), 7221−7228.
(32) Hardin, R. H.; Sloane, N. J. A.; Smith, W. D. *Tables of spherical codes with icosahedral symmetry*, published electronically at http://NeilSloane.com/icosahedral.codes/.
(33) Kim, J. M.; Phillips, R. J. Dissipative particle dynamics simulation of flow around spheres and cylinders at finite Reynolds numbers. *Chem. Eng. Sci.* **2004**, *59* (20), 4155−4168.
(34) Chen, S.; Phan-Thien, N.; Khoo, B. C.; Fan, X. J. Flow around spheres by dissipative particle dynamics. *Phys. Fluids* **2006**, *18* (10), 103605.
(35) Johnson, K.; Kendall, K.; Roberts, A. Surface energy and the contact of elastic solids. *Proc. R. Soc. London, Ser. A* **1971**, *324* (1558), 301−313.
(36) Füchslin, R. M.; Fellermann, H.; Eriksson, A.; Ziock, H.-J. Coarse graining and scaling in dissipative particle dynamics. *J. Chem. Phys.* **2009**, *130* (21), 214102.
(37) Zhao, Y.; Cho, S. K. Microparticle sampling by electrowetting-actuated droplet sweeping. *Lab Chip* **2006**, *6* (1), 137−144.

DOI: 10.1021/acs.langmuir.5b02011
Langmuir 2015, 31, 9636−9645